Generation of coherent spin-wave modes in Yttrium Iron Garnet microdiscs by spin-orbit torque

Martin Collet, Xavier De Milly, Olivier D'Allivy-Kelly, Vladimir V. Naletov,
Rozenn Bernard, Paolo Bortolotti, Vladislav Demidov, Sergej Demokritov,
Jose Luis Prieto, Manuel Muñoz, et al.

Generation of coherent spin-wave modes in Yttrium Iron Garnet microdiscs by spin-orbit torque

M. Collet,[1] X. de Milly,[2] O. d'Allivy Kelly,[1] V. V. Naletov,[3, 4] R. Bernard,[1] P. Bortolotti,[1] V. E. Demidov,[5] S. O. Demokritov,[5, 6] J. L. Prieto,[7] M. Muñoz,[8] V. Cros,[1] A. Anane,[1] G. de Loubens,[2] and O. Klein[3]

[1] *Unité Mixte de Physique CNRS/Thales and Université Paris Sud 11, 1 av. Fresnel, 91767 Palaiseau, France*
[2] *Service de Physique de l'État Condensé (CNRS UMR 3680), CEA Saclay, 91191 Gif-sur-Yvette, France*
[3] *INAC-SPINTEC, CEA/CNRS and Univ. Grenoble Alpes, 38000 Grenoble, France*
[4] *Institute of Physics, Kazan Federal University, Kazan 420008, Russian Federation*
[5] *Department of Physics, University of Muenster, 48149 Muenster, Germany*
[6] *Institute of Metal Physics, Ural Division of RAS, Yekaterinburg 620041, Russian Federation*
[7] *Instituto de Sistemas Optoelectrónicos y Microtecnología (UPM), Madrid 28040, Spain*
[8] *Instituto de Microelectrónica de Madrid (CNM, CSIC), Madrid 28760, Spain*
(Dated: April 7, 2015)

Spin-orbit effects[1–4] have the potential of radically changing the field of spintronics by allowing transfer of spin angular momentum to a whole new class of materials. In a seminal letter to Nature[5], Kajiwara *et al.* showed that by depositing Platinum (Pt, a normal metal) on top of a 1.3 μm thick Yttrium Iron Garnet (YIG, a magnetic insulator), one could effectively transfer spin angular momentum through the interface between these two different materials. The outstanding feature was the detection of auto-oscillation of the YIG when enough dc current was passed in the Pt. This finding has created a great excitement in the community for two reasons: first, one could control electronically the damping of insulators, which can offer improved properties compared to metals, and here YIG has the lowest damping known in nature; second, the damping compensation could be achieved on very large objects, a particularly relevant point for the field of magnonics[6,7] whose aim is to use spin-waves as carriers of information. However, the degree of coherence of the observed auto-oscillations has not been addressed in ref.[5]. In this work, we emphasize the key role of quasi-degenerate spin-wave modes, which increase the threshold current. This requires to reduce both the thickness and lateral size in order to reach full damping compensation[8], and we show clear evidence of coherent spin-orbit torque induced auto-oscillation in micron-sized YIG discs of thickness 20 nm.

When spin transfer effects were first introduced by Slonczweski and Berger in 1996[9,10], the authors immediately recognized that the striking signature of the transfer process would be the emission of microwave radiation when the system is pumped out of equilibrium by a dc current. Since the spin transfer torque on the magnetisation is collinear to the damping torque, there is an instability threshold when the natural damping is fully compensated by the external flow of angular momentum, leading to spin-wave amplification through stimulated emission. Using analogy to light, the effect was called SWASER[10], where SW stands for spin-wave. Until 2010, all SWASER devices required a charge current perpendicular to the plane to transfer angular momentum between different magnetic layers[9,10]. This implied that the effect was restricted to conducting materials. The situation has radically changed since spin-orbit effects such as the spin Hall effect (SHE)[11,12] are used to produce spin currents in normal metals. Here a right hand side rule links the deflected direction of the electron and the orientation of its spin. This allows the creation of a pure spin current transversely to the charge current, with an efficiency given by the spin Hall angle Θ_{SH}. Using a metal with large Θ_{SH}, such as Pt, a charge current flowing in plane generates a pure spin current flowing perpendicular to the plane, which can eventually be transferred

through an interface with ferromagnetic metals, resulting in the coherent emission of spin-waves[13], but also with non-metals such as YIG[5].

The microscopic mechanisms of transfer of angular momentum between a normal metal and a ferromagnetic layer are quite different depending on the latter being metallic or not. In the first case, electrons in each layer have the possibility to penetrate the other one, whereas in the second case the transfer takes place exactly and solely at the interface. It is thus much more sensitive to the imperfection of the interface. Still, a direct experimental evidence that spin current can indeed cross such an hybrid interface is through the so-called spin pumping effect[14]: adding a normal metal on top of YIG increases its ferromagnetic resonance (FMR) linewidth[15], which is due to the new relaxation channel at the interface through which angular momentum can escape and get absorbed in the metal. This effect being interfacial, the broadening scales as $1/t_{\mathrm{YIG}}$, where t_{YIG} is the thickness of YIG. Even for YIG, whose natural linewidth is only a few Oersted at 10 GHz, it is hardly observable if t_{YIG} exceeds a couple hundreds of nanometers. For these thick films though, the spin pumping can still be detected through inverse spin Hall effect (ISHE). In a normal metal with strong spin-orbit interaction, the pumped spin current is converted into a transverse charge current.

This generates a voltage proportional to the length of the sample across the metal, which can easily reach several tens of microvolts in millimeter-sized samples. Since the first experiment by Kajiwara *et al.*[5], many studies reported the ISHE detection of FMR using different metals on YIG layers[16–18], hereby providing clear evidence of at least partial transparency of the hybrid YIG|metal interfaces to spin currents. Due to Onsager relations, these results made the community confident that a spin current could thus be injected from metals to YIG and lead to the SWASER effect.

From the beginning it was anticipated that the key to observe auto-oscillations in non-metals was to reduce the threshold current. The first venue is of course to choose a material whose natural damping is very low. In this respect YIG is the optimal choice. The second thing is to reduce the thickness since the spin-orbit torque (SOT) is an interfacial effect. This triggered an effort in the fabrication of ultra-thin films of YIG of very high dynamical quality[19,20]. For 20 nm thick YIG films with damping constant as low as $\alpha = 2.3 \cdot 10^{-4}$, a striking result was that there were no evidence of auto-oscillations in millimeter-sized samples at the highest dc current possible in the top Pt layer[20], *i.e.*, before it evaporates. It is worth mentioning at this point that reducing further the thickness or the damping parameter of such ultra-thin YIG films[21] does not help anymore in decreasing the threshold current, as the relevant value of the damping is that of the YIG|Pt hybrid, which ends up to be completely dominated by the spin-pumping contribution.

But most notably, none of these high-quality ultra-thin YIG films display a purely homogeneous FMR line. The reason for that is well known. In such extended films, there are many degenerate modes with the main, uniform FMR mode, which through the process of two-magnon scattering broaden the linewidth[22,23]. A striking evidence of these degenerate modes can be obtained by parametrically pumping the SW modes. It reveals an uncountable number of modes which are at the same energy as the FMR mode[24]. Any threshold instability will be affected by the presence of those modes, as learnt from LASERs where mode competition is known to have a strong influence on the emission threshold[25]. Thus, the next natural step was to reduce as well the lateral size in order to lift the degeneracy between modes through confinement. The first microstructures of YIG appeared revealing that the patterning indeed narrowed the linewidth through a decrease of the inhomogeneous part[26]. The effect is clear in the perpendicular geometry, where magnon-magnon processes are suppressed owing to the fact that the FMR mode lies at the bottom of the SW dispersion relation. However, this is not the case in the parallel geometry where the FMR mode is not the lowest energy SW mode. Even then, we showed that the linewidth in a micron-sized YIG|Pt disc could be still tuned thanks to SOT[8]. In the following, we describe the direct electrical detection of auto-oscillations in similar samples and show that the threshold current is increased
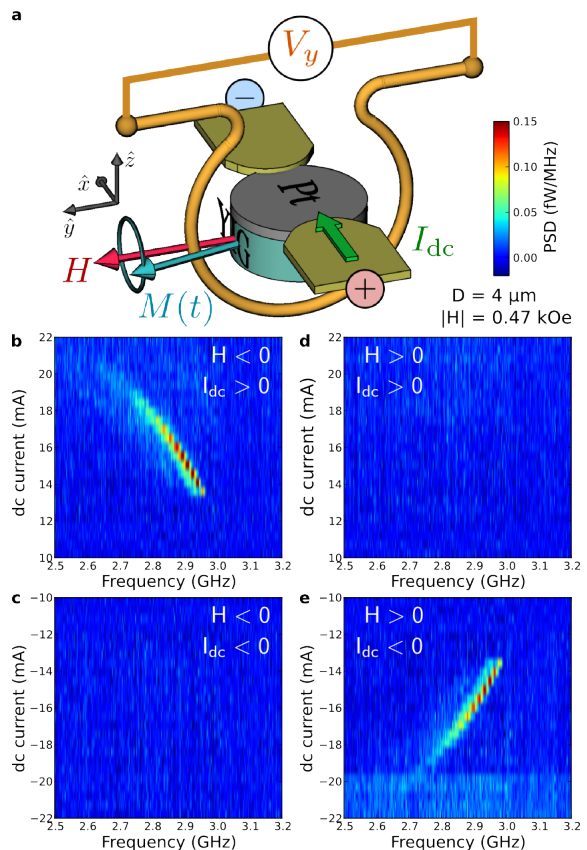

FIG. 1. **Inductive detection of auto-oscillations in a YIG|Pt microdisc. a**, Sketch of the sample and measurement configuration. The bias field H is oriented transversely to the dc current I_{dc} flowing in Pt. The inductive voltage V_y produced in the antenna by the precession of the YIG magnetisation is amplified and monitored by a spectrum analyser. **b–e**, Power spectral density maps measured at fixed $|H| = 0.47$ kOe and variable I_{dc}. The four quadrants correspond to different possible polarities of H and I_{dc}.

by the presence of quasi-degenerate SW modes.

We study magnetic microdiscs with diameter 2 μm and 4 μm which are fabricated based on a hybrid YIG(20 nm)|Pt(8 nm) bilayer. The 20 nm thick YIG layer is grown by pulsed laser deposition[20] and the 8 nm thick Pt layer is sputtered on top of it[27]. Their physical parameters are summarized in Table I. We stress that the extended YIG film is characterized by a low Gilbert damping parameter $\alpha_0 = (4.8 \pm 0.5) \cdot 10^{-4}$ and a remarkably small inhomogeneous contribution to the linewidth, $\Delta H_0 = 1.1 \pm 0.3$ Oe. Each microdisc is connected to electrodes enabling the injection of a dc current I_{dc} in the Pt layer, and a microwave antenna is defined around it to obtain an inductive coupling with the YIG magnetisation, as shown schematically in Fig. 1a.

First, we monitor with a spectrum analyser the voltage produced in the antenna by potential auto-oscillations of the 4 μm YIG disc as a function of the dc current I_{dc} injected in Pt. The in-plane magnetic field $H = 0.47$ kOe

TABLE I. Physical parameters of the Pt and bare YIG layers, and of the hybrid YIG|Pt bilayer.

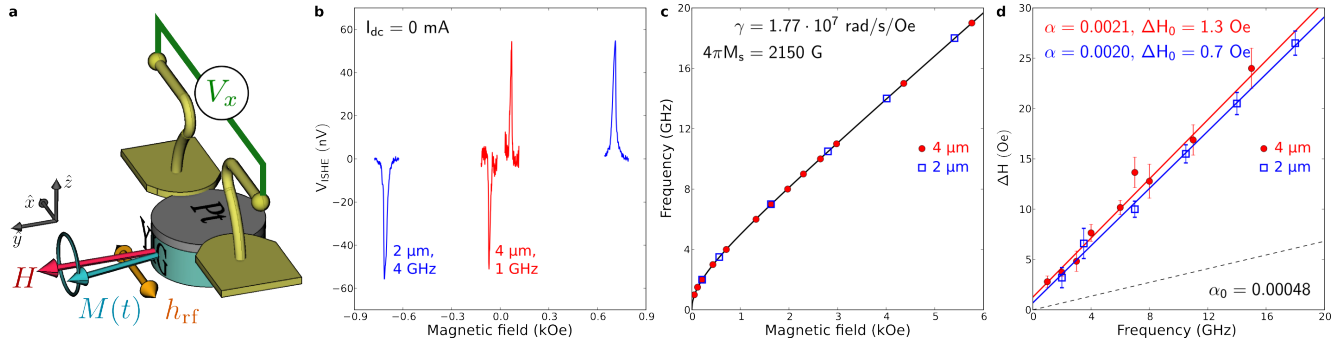| Pt	t_{Pt} (nm)	ρ ($\mu\Omega$.cm)	λ_{SD} (nm)	Θ_{SH}
from ref.[27]	8	17.3 ± 0.6	3.4 ± 0.4	0.056 ± 0.010
YIG	t_{YIG} (nm)	α_0	$4\pi M_s$ (G)	γ (10^7 rad.s^{-1}.G^{-1})
this study	20	$(4.8 \pm 0.5) \cdot 10^{-4}$	2150 ± 50	1.770 ± 0.005
YIG|Pt	$t_{YIG}|t_{Pt}$ (nm)	α	$g_{\uparrow\downarrow}$ (10^{18} m^{-2})	T
this study	20|8	$(2.05 \pm 0.1) \cdot 10^{-3}$	3.6 ± 0.5	0.2 ± 0.05

FIG. 2. **ISHE-detected FMR spectroscopy in YIG|Pt microdiscs. a**, Sketch of the sample and measurement configuration. The bias field H is oriented perpendicularly to the Pt electrode and to the excitation field h_{rf} produced by the antenna at fixed microwave frequency. The dc voltage V_x across Pt is monitored as a function of the magnetic field. **b**, ISHE-detected FMR spectra of the 4 μm and 2 μm YIG(20 nm)|Pt(8 nm) discs at 1 GHz and 4 GHz, respectively. **c**, Dispersion relation of the main FMR mode of the microdiscs. The continuous line is a fit to the Kittel law. **d**, Frequency dependence of the FMR linewidth in the two microdiscs. The vertical bars show the mean squared error of the lorentzian fits. The continuous lines are linear fits to the data. The dashed line shows the homogeneous contribution of the bare YIG.

is applied in a transverse direction with respect to I_{dc}, as shown in Fig. 1a. This is the most favorable configuration to compensate the damping and obtain auto-oscillations in YIG, as spins accumulated at the YIG|Pt interface due to SHE in Pt will be collinear to its magnetisation. Color plots of the inductive signal measured as a function of the relative polarities of H and I_{dc} are presented in Fig. 1b–e. At $H < 0$, we observe in the power spectral density (PSD) a peak which starts at around 2.95 GHz and 13 mA and then shifts towards lower frequency as I_{dc} is increased (Fig. 1b), a clear signature that spin transfer occurs through the YIG|Pt interface. The linewidth of the emission peak, lying in the 10–20 MHz range for $13 < I_{dc} < 17$ mA, also proves the coherent nature of the detected signal. An identical behaviour is observed at $H > 0$ and $I_{dc} < 0$ (Fig. 1d). In contrast, the PSD remains flat in the two other cases (Fig. 1c–d). Therefore, an auto-oscillation signal is detected only if $H \cdot I_{dc} < 0$, in agreement with the expected symmetry of SHE.

In order to characterize the flow of angular momentum across the YIG|Pt interface, we now perform ISHE-detected FMR spectroscopy on our microdiscs. The configuration of this experiment is similar to the previous case, but now the antenna generates a uniform microwave field h_{rf} to excite the FMR of YIG while the dc voltage across Pt is monitored at zero current (see Fig. 2a). In other words, we perform the reciprocal experiment of the

one presented in Fig. 1. As described in the introduction, a voltage V_{ISHE} develops across Pt when the FMR conditions are met in YIG. This voltage changes sign as the field is reversed, which is expected from the symmetry of ISHE, and shown in Fig. 2b, where the FMR spectra of the 4 μm and 2 μm microdiscs are respectively detected at 1 GHz and 4 GHz. We also note that for a given field polarity, the product between V_{ISHE} and I_{dc} must be negative to compensate the damping[8], which enables to observe auto-oscillations in Fig. 1.

From these ISHE measurements, the dispersion relation and frequency dependence of the full linewidth at half maximum of the main FMR mode can be determined, as shown in Figs. 2c and 2d, respectively. The dispersion relation follows the expected Kittel law. The damping parameters of the 4 μm and 2 μm microdiscs, extracted from linear fits to the data, $\Delta H = 2\alpha\omega/\gamma + \Delta H_0$ (continuous lines in Fig. 2d, ω is the pulsation frequency and γ the gyromagnetic ratio), are found to be similar with an average value of $\alpha = (2.05 \pm 0.1) \cdot 10^{-3}$. The small inhomogeneous contribution to the linewidth observed in both microdiscs, $\Delta H_0 = 1.3 \pm 0.4$ Oe and $\Delta H_0 = 0.7 \pm 0.4$ Oe, respectively, decreases with the diameter and is attributed to the presence of several unresolved modes within the resonance line[8]. In order to emphasize the increase of damping due to Pt, we have reported in Fig. 2d the broadening produced by the homogeneous contribution of the bare YIG using a dashed

line. The observed increase of damping is due to spin pumping[14,15],

$$\alpha - \alpha_0 = g_{\uparrow\downarrow}\frac{\gamma\hbar}{4\pi M_s t_{\text{YIG}}} \, , \qquad (1)$$

where $\hbar$ is the reduced Planck constant, M_s the saturation magnetisation and $g_{\uparrow\downarrow}$ the spin-mixing conductance of the YIG|Pt interface. This allows us to extract $g_{\uparrow\downarrow} = (3.6\pm0.5)\cdot10^{18}$ m^{-2}, which lies in the same window as previously reported values[26,28]. From the spin-mixing conductance $g_{\uparrow\downarrow}$, the spin diffusion length λ_{SD} and the resistivity ρ of the Pt layer, we can also calculate the transparency of the YIG|Pt interface to spin current[29], $T = 0.2 \pm 0.05$. The physical parameters extracted for the YIG|Pt hybrid bilayer are summarized in the last raw of Table I.

To gain further insight about the origin of the auto-oscillation signal, we now monitor how the auto-oscillations of the 4 μm disc evolve as the angle ϕ between the in-plane bias field fixed to $H = 0.47$ kOe and the dc current I_{dc} is varied from 30° to 150°. The results are summarized in Fig. 3. Pannels b–d show the auto-oscillation voltages detected in the antenna (V_y) and across the Pt electrode (V_x). At $\phi = 90°$, the auto-oscillation signal is only visible in the V_y channel. At $\phi = 60°$, both V_x and V_y channels exhibit the auto-oscillation peak. At $\phi = 40°$, it almost vanishes in V_y, while it slightly increases in V_x. The normalized signals as a function of ϕ are plotted in Fig. 3e. The Pt electrode and antenna loop being oriented perpendicularly to each other (see Fig. 3a), the ac flux due to the precession of magnetisation picked up by each of them respectively varies as $\cos\phi$ and $\sin\phi$ (dashed lines in Fig. 3e).

More importantly, this study of angle dependence also allows us to extract the threshold current for auto-oscillations as a function of ϕ. As ϕ deviates from the optimal orientation 90°, the absolute value of the threshold current rapidly increases, see Fig. 3f. In fact, the SOT acting on the oscillating part $\mathbf{m}$ of the magnetisation scales as $\mathbf{m} \times \mathbf{s} \times \mathbf{m} \propto \sin\phi$, where $\mathbf{s}$ is the spin polarisation of the dc spin current produced by SHE in Pt at the YIG|Pt interface. Therefore, the expected threshold current scales as $1/\sin\phi$, which is plotted as a dashed line in Fig. 3f, in very good agreement with the data.

In summary, the results reported in Figs. 1 and 3 unambiguously demonstrate that the auto-oscillations observed in our hybrid YIG|Pt discs result from the action of SOT produced by I_{dc}. We have also shown that they correspond to the reverse effect of the spin pumping mechanism illustrated in Fig. 2d and its detection through ISHE in Fig. 2b.

In the last part of this letter, we analyse quantitatively the main features of auto-oscillations, which allows us to determine their nature and to understand the role of quasi-degenerate SW modes in the SOT driven dynamics.

For this, we compare the auto-oscillations observed in the 4 μm and 2 μm microdiscs. Figs. 4a and 4b respectively present the inductive signal V_y detected in the
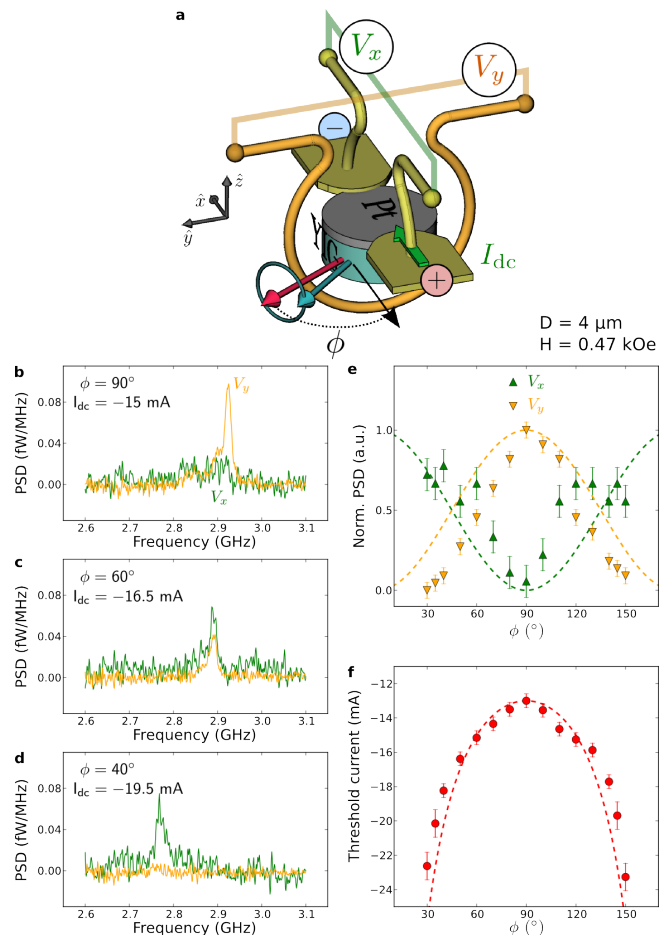

FIG. 3. **Auto-oscillations as a function of the angle between the dc current and the bias field. a**, Sketch of the sample and measurement configuration. The bias field H is oriented at an angle ϕ with the dc current I_{dc} in the Pt. The precession of the YIG magnetisation induces voltages V_x in the antenna and V_y across Pt, which are amplified and monitored by spectrum analysers. **b–d**, V_x and V_y at $H = 0.47$ kOe for three different angles ϕ. **e**, Dependence of the normalized signals in both circuits and **f**, of the threshold current for auto-oscillations on ϕ. Dashed lines show the expected angular dependences.

antenna coupled to these two discs as a function of I_{dc}. The configuration is the same as depicted in Fig. 1a, with a slightly larger bias field set to $H = 0.65$ kOe. One can clearly see a peak appearing in the PSD close to 3.6 GHz in both cases, at a threshold current of about -13.5 mA in the 4 μm disc and -7.4 mA in the 2 μm disc. These two values correspond to a similar threshold current density in both samples of $(4.4\pm0.2)\cdot10^{11}$ A.m^{-2}, in agreement with our previous study[8]. As the dc current is varied towards more negative values, the peaks shift towards lower frequency (Fig. 4c), at a rate which is twice faster in the smaller disc. This frequency shift is mainly due to linear and quadratic contributions in I_{dc} of Oersted field and Joule heating, respectively[8] (from the Pt resistance, the maximal temperature increase in both
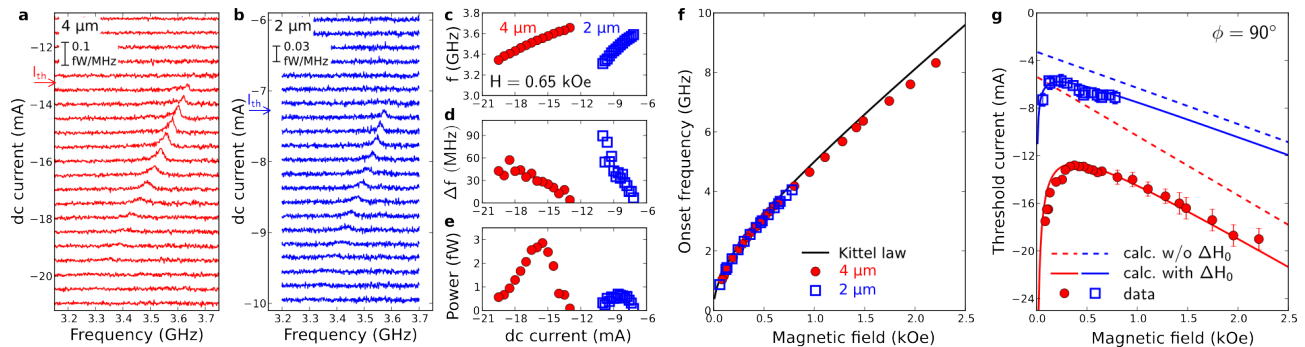
FIG. 4. **Quantitative analysis of auto-oscillations in YIG|Pt microdiscs**. **a**, Inductive voltage V_y produced by auto-oscillations in the 4 μm and **b**, 2 μm YIG|Pt discs as a function of the dc current I_{dc} in the Pt. The experimental configuration is the same as in Fig. 1a, with the bias field fixed to $H = 0.65$ kOe. **c**, Auto-oscillation frequency, **d**, linewidth and **e**, integrated power *vs.* I_{dc}. **f**, Dependence of the onset frequency and **g**, of the threshold current on the applied field in both discs. Expectations taking into account only the homogeneous linewidth or the total linewidth are respectively shown by dashed and continuous lines.

samples is estimated to be $+40°$C). At the same time, the signal first rapidly increases in amplitude, reaches a maximum, and then, more surprisingly, drops until it cannot be detected anymore, as seen in Fig. 4e, which plots the integrated power *vs.* I_{dc}. The maximum of power measured in the 4 μm disc (2.9 fW) is four times larger than the one measured in the 2 μm disc (0.7 fW), which is due to the inductive origin of V_y. The latter can be estimated from geometrical considerations, $V_y = \eta(\omega\mu_0 D t_{YIG} M_s \sin\theta)/2$. Here μ_0 is the magnetic constant, D the diameter of the disc and θ the angle of uniform precession (the prefactor $\eta \simeq 0.1$ accounts for microwave losses and impedance mismatch in the measured frequency range with our microwave circuit). For the same θ, the inductive voltage produced by the 4 μm disc is thus twice larger than by one produced by the 2 μm disc, hence the ratio four in power. Moreover, the maximal angle of precession reached by auto-oscillations is found to be about $1°$ in both microdiscs[8]. Finally, the disappearance of the signal as I_{dc} gets more negative is accompanied by a continuous broadening of the linewidth, which increases from a few MHz to several tens of MHz (Fig. 4d). This rather large auto-oscillation linewidth is also consistent with a small precession angle, *i.e.*, a small stored energy in the YIG oscillator[30].

By repeating the same analysis as a function of H, we can determine the bias field dependence of the auto-oscillations in both microdiscs. The onset frequency and threshold current at which auto-oscillations start are plotted in Figs. 4f and 4g, respectively. The onset frequency in the 4 μm and 2 μm microdiscs is identical and closely follows the dispersion relation of the main FMR mode plotted as a continuous line. The small redshift towards lower frequency, which increases with the applied field, is ascribed to the Joule heating and Oersted field induced by I_{dc} (the Kittel law in Figs. 2c and 4f is obtained at $I_{dc} = 0$ mA). We also note that the main FMR mode is the one which couples the most efficiently to our inductive electrical detection, because it is the most uniform.

Hence, we conclude that the detected auto-oscillations are due to the destabilisation of this mode by SOT.

In order to reach auto-oscillations, the additional damping term due to SOT has to compensate the natural relaxation rate Γ_r in YIG. Given the transparency T of the YIG|Pt interface and the spin Hall angle Θ_{SH} in Pt, this condition writes:

$$T\Theta_{SH}\frac{\hbar}{2e}\frac{\gamma}{t_{YIG}M_s}\frac{I_{th}}{t_{Pt}D} = -\Gamma_r, \qquad (2)$$

where $t_{Pt}D$ is the section of the Pt layer. The homogeneous contribution to Γ_r is given by the Gilbert damping rate, which for the in-plane geometry is:

$$\Gamma_G = \alpha\gamma(H + 2\pi M_s). \qquad (3)$$

We remind that this expression is obtained by converting the field linewidth to frequency linewidth through $\Delta\omega = \Delta H(\partial\omega/\partial H)$. If only the homogeneous contribution to the linewidth is taken into account, the threshold current I_{th} is thus expected to depend linearly on H, as shown by the dashed lines plotted in Fig. 4g using Eqs. 2 and 3, and the parameters listed in Table I (the only adjustment made is for the 4 μm disc, where the calculated I_{th} has been reduced by 20% in order to reproduce asymptotically the experimental slope of I_{th} *vs.* H). It qualitatively explains the dependence of I_{th} at large bias field in both microdiscs, but underestimates its value and fails to reproduce the optimum observed at low bias field.

To understand this behaviour, the finite inhomogeneous contribution to the linewidth ΔH_0 measured in Fig. 2d should be considered as well. In fact, this contribution dominates the full linewidth at low bias field. In that case, the expression of the relaxation rate writes:

$$\Gamma_r = \Gamma_G + \gamma\frac{\Delta H_0}{2}\frac{H + 2\pi M_s}{\sqrt{H(H + 4\pi M_s)}}. \qquad (4)$$

The form of the last term in Eq. 4 is due to the Kittel dispersion relation and is responsible for the existence

of the optimum in I_{th} at $H \neq 0$. Using the value of $\Delta H_0 = 0.7$ Oe extracted in Fig. 2d for the 2 μm disc in Eq. 4 in combination with Eq. 2, the continuous blue line of Fig. 4g is calculated, in very good agreement with the experimental data. To get such an agreement for the 4 μm disc, ΔH_0 has to be increased by 25% compared to the value determined in Fig. 2d. In this case, both the position of the optimum (observed at $H \simeq 0.3 - 0.5$ kOe) and the exact value of I_{th} are also well reproduced for the 4 μm disc, as shown by the continuous red line in Fig. 4g.

Hence, it turns out that quasi-degenerate SW modes, which are responsible for the inhomogeneous contribution to the linewidth, strongly affect the exact value and detailed dependence *vs.* H of I_{th}. In fact, it is the total linewidth that truly quantifies the losses of a magnetic device regardless of the nature and number of microscopic mechanisms involved. Even in structures with micron-sized lateral dimensions, there still exist a few quasi-degenerate SW modes as evidenced by the finite ΔH_0 observed in Fig. 2d. Due to magnon-magnon scattering, they are linearly coupled to the main FMR mode, which as a result has its effective damping increased, along with the threshold current. The presence of these SW modes is also known to play a crucial role in SOT driven dynamics. The strongly non-equilibrium distribution of SWs promoted by SOT in combination with nonlinear interactions between modes can lead to mode competition, which might even prevent auto-oscillations to start[31]. We believe that the observed behaviours of the integrated power (Fig. 4d) and linewidth (Fig. 4e) *vs.* I_{dc} are reminiscent of the presence of these quasi-degenerate SW modes. A meaningful interpretation of these experimental results is that as the FMR mode starts to auto-oscillate and to grow in amplitude as the dc current is increased above the threshold, its coupling to other SW modes – whose amplitudes also grow due to SOT – becomes larger, which makes the flow of energy out of the FMR mode more efficient. This reduces the inductive signal, as non-uniform SW modes are poorly coupled to our inductive detection scheme. At the same time, it enhances the auto-oscillation linewidth, which reflects this additional nonlinear relaxation channel.

The smaller inhomogeneous linewidth in the 2 μm disc (Fig. 2d) results in a field dependence of the threshold current closer to the one expected for the purely homogeneous case (Fig. 4g). This indicates that reducing further the lateral size of the microstructure will allow to completly lift the quasi-degeneracy between spin-wave modes[26], as predicted by micromagnetic simulations, which show that this is obtained for lateral sizes smaller than 1 μm. This could extend the stability of the auto-oscillation for the FMR mode, and experimental techniques capable of detecting SWs in nanostructures[8,31] should be used to probe this transition. Very importantly for the field of magnonics, it was recently shown that this constraint on confinement could be relaxed in one dimen-

sion such as to produce a propagation stripe[32]. Other strategies might consist in using specific non-uniform SW modes or to engineer the SW spectrum using topological singularities such as vortices, or bubbles, which could be most relevant to design active magnonics computational circuits.

METHODS

Samples – Details of the PLD growth of the YIG layer can be found in ref.[20]. Its dynamical properties have been determined by broadband FMR measurements. The transport parameters of the 8 nm thick Pt layer deposited on top by magnetron sputtering have been determined in a previous study[27]. The YIG|Pt microdiscs are defined by e-beam lithography, as well as the Au(80 nm)|Ti(20 nm) electrodes – separated by 1 μm from each other – which contact them. This electrical circuit is insulated by a 300 nm thick SiO_2 layer, and a broadband microwave antenna made of 250 nm thick Au with a 5 μm wide constriction is defined on top of each disc by optical lithography.

Measurements – The samples are mounted between the poles of an electromagnet which can be rotated to vary the angle ϕ shown in Fig. 3a. Two 50 Ω matched picoprobes are used to connect to the microwave antenna and to the electrodes which contact the Pt layer. The latter are connected to a dc current source through a bias-tee. To perform ISHE-detected FMR measurements, a microwave synthesizer is connected to the microwave antenna, and the output power is turned on and off at a modulation frequency of 9 kHz. The voltage across Pt is measured by a lock-in after a low-noise preamplifier (gain 100). For the detection of auto-oscillations, high-frequency low-noise amplifiers are used (gain 33 dB to 39 dB, depending on the frequency range). Two spectrum analysers simultaneously monitor in the frequency domain the voltages V_x and V_y across the Pt layer and in the microwave antenna, respectively (Fig. 3a). The resolution bandwidth employed in the measurements is set to 1 MHz.

[1] A. Manchon and S. Zhang, Phys. Rev. B **79**, 094422 (2009).

[2] I. M. Miron, K. Garello, G. Gaudin, P.-J. Zermatten, M. V. Costache, S. Auffret, S. Bandiera, B. Rodmacq, A. Schuhl, and P. Gambardella, Nature **476**, 189 (2011).

[3] J.-C. Rojas-Sánchez, L. Vila, G. Desfonds, S. Gambarelli, J. P. Attan, J. M. D. Teresa, C. Magn, and A. Fert, Nature Comm. **4**, 2944 (2013).

[4] A. R. Mellnik, J. S. Lee, A. Richardella, J. L. Grab, P. J. Mintun, M. H. Fischer, A. Vaezi, A. Manchon, E.-A. Kim, N. Samarth, and D. C. Ralph, Nature **511**, 449 (2014).

[5] Y. Kajiwara, K. Harii, S. Takahashi, J. Ohe, K. Uchida, M. Mizuguchi, H. Umezawa, H. Kawai, K. Ando, K. Takanashi, S. Maekawa, and E. Saitoh, Nature **464**, 262 (2010).

[6] V. V. Kruglyak, S. O. Demokritov, and D. Grundler, J. Phys. D **43**, 264001 (2010).

[7] A. A. Serga, A. V. Chumak, and B. Hillebrands, J. Phys. D **43**, 264002 (2010).

[8] A. Hamadeh, O. d'Allivy Kelly, C. Hahn, H. Meley, R. Bernard, A. H. Molpeceres, V. V. Naletov, M. Viret, A. Anane, V. Cros, S. O. Demokritov, J. L. Prieto, M. Muñoz, G. de Loubens, and O. Klein, Phys. Rev. Lett. **113**, 197203 (2014).

[9] J. Slonczewski, J. Magn. Magn. Mater. **159**, L1 (1996).

[10] L. Berger, Phys. Rev. B **54**, 9353 (1996).

[11] M. I. Dyakonov and V. I. Perel, JETP Lett. **13**, 467 (1971).

[12] J. E. Hirsch, Phys. Rev. Lett. **83**, 1834 (1999).

[13] V. Demidov, S. Urazhdin, H. Ulrichs, V. Tiberkevich, A. Slavin, D. Baither, G. Schmitz, and S. O. Demokritov, Nature Mater. **11**, 1028 (2012).

[14] Y. Tserkovnyak, A. Brataas, G. E. W. Bauer, and B. I. Halperin, Rev. Mod. Phys. **77**, 1375 (2005).

[15] B. Heinrich, C. Burrowes, E. Montoya, B. Kardasz, E. Girt, Y.-Y. Song, Y. Sun, and M. Wu, Phys. Rev. Lett. **107**, 066604 (2011).

[16] C. Hahn, G. de Loubens, O. Klein, M. Viret, V. V. Naletov, and J. Ben Youssef, Phys. Rev. B **87**, 174417 (2013).

[17] J. B. S. Mendes, R. O. Cunha, O. Alves Santos, P. R. T. Ribeiro, F. L. A. Machado, R. L. Rodríguez-Suárez, A. Azevedo, and S. M. Rezende, Phys. Rev. B **89**, 140406 (2014).

[18] H. L. Wang, C. H. Du, Y. Pu, R. Adur, P. C. Hammel, and F. Y. Yang, Phys. Rev. Lett. **112**, 197201 (2014).

[19] Y. Sun, Y.-Y. Song, H. Chang, M. Kabatek, M. Jantz, W. Schneider, M. Wu, H. Schultheiss, and A. Hoffmann, Appl. Phys. Lett. **101**, 152405 (2012).

[20] O. d'Allivy Kelly, A. Anane, R. Bernard, J. Ben Youssef, C. Hahn, A. H. Molpeceres, C. Carretero, E. Jacquet, C. Deranlot, P. Bortolotti, R. Lebourgeois, J.-C. Mage, G. de Loubens, O. Klein, V. Cros, and A. Fert, Appl. Phys. Lett. **103**, 082408 (2013).

[21] H. Chang, P. Li, W. Zhang, T. Liu, A. Hoffmann, L. Deng, and M. Wu, IEEE Magn. Lett. **5**, 1 (2014).

[22] R. Arias and D. L. Mills, Phys. Rev. B **60**, 7395 (1999).

[23] R. McMichael and P. Krivosik, IEEE Trans. Magn. **40**, 2 (2004).

[24] C. Hahn, G. de Loubens, M. Viret, O. Klein, V. V. Naletov, and J. Ben Youssef, Phys. Rev. Lett. **111**, 217204 (2013).

[25] L. V. Asryan and R. A. Suris, Semiconductor Science and Technology **11**, 554 (1996).

[26] C. Hahn, V. V. Naletov, G. de Loubens, O. Klein, O. d'Allivy Kelly, A. Anane, R. Bernard, E. Jacquet, P. Bortolotti, V. Cros, J. L. Prieto, and M. Muñoz, Appl. Phys. Lett. **104**, 152410 (2014).

[27] J.-C. Rojas-Sánchez, N. Reyren, P. Laczkowski, W. Savero, J.-P. Attané, C. Deranlot, M. Jamet, J.-M. George, L. Vila, and H. Jaffrès, Phys. Rev. Lett. **112**, 106602 (2014).

[28] M. B. Jungfleisch, V. Lauer, R. Neb, A. V. Chumak, and B. Hillebrands, Appl. Phys. Lett. **103**, 022411 (2013).

[29] Y.-T. Chen, S. Takahashi, H. Nakayama, M. Althammer, S. T. B. Goennenwein, E. Saitoh, and G. E. W. Bauer, Phys. Rev. B **87**, 144411 (2013).

[30] J.-V. Kim, V. Tiberkevich, and A. N. Slavin, Phys. Rev. Lett. **100**, 017207 (2008).

[31] V. E. Demidov, S. Urazhdin, E. R. J. Edwards, M. D. Stiles, R. D. McMichael, and S. O. Demokritov, Phys. Rev. Lett. **107**, 107204 (2011).

[32] Z. Duan, A. Smith, L. Yang, B. Youngblood, J. Lindner, V. E. Demidov, S. O. Demokritov, and I. N. Krivorotov, Nature Comm. **5**, 5616 (2014).